Electronic supplementary information: Population dependence of THz charge carrier mobility and non-Drude-like behavior in short semiconductor nanowires

Alexander W. Achtstein,* Nina Owschimikow, and Michael T. Quick

Institute of Optics and Atomic Physics, Technical University of Berlin, Strasse des 17. Juni 135, 10623 Berlin, Germany

E-mail: achtstein@tu-berlin.de

Fax: +49(0)30 31421079

Contents

S1 Methods

Charge carriers are described as quantized particles in an infinite 3D potential well governing the following wave functions in terms of the quantum numbers n, m and j:

$$\Psi_{n,m,j} = \sqrt{\frac{8}{L_x L_y L}} \sin\left(\frac{n\pi x}{L_x}\right) \sin\left(\frac{m\pi y}{L_y}\right) \sin\left(\frac{j\pi z}{L}\right) \tag{S1}$$

with the wire extending from z = 0 to L in z-direction and from zero to $L_{x,y}$ in perpendicular directions. The wires are assumed to be much longer than their thickness $L_{x,y}$. As the wire's transversal dimensions are considered much smaller than the length, we need to consider only transition elements in z-direction for the mobility since the transition energies in x- or y-direction are much higher in energy than the THz photon energy $\hbar\omega$. Hence, due to strong off-resonance the probability of perpendicular transitions is very low due to the energy denominator in Equation 1 (main text). In contrast, in the extended z-direction the (lowest) energy level spacing is in the meV range (18 meV for a 20 nm wire length with $m_e = 0.31$ m_0 and hence near resonant to typical THz photons of 0.1 to 3 THz (0.4 to 12 meV)). For these reasons we can safely neglect x- and y-related intraband transitions for thin rods and wires and concentrate on the $i \rightarrow j$ transitions in z-direction. However, the product ansatz in Equation S1 takes care of a proper evaluation of the matrix elements in Equation 1 from the main text, as the x- and y-direction integrals just result in unity factors once the integral is factorized, since the quantum state $|n = 1, m = 1, j\rangle$ of the charge maintains its lowest x and y quantum state. The corresponding full energetic description is given by

$$E_{n,m,j} = \frac{\pi^2 \hbar^2}{2m^*} \left((n/L_x)^2 + (m/L_y)^2 + (j/L)^2 \right). \tag{S2}$$

Again, as $L = L_z \gg L_x$, L_y, we will be only concerned with transitions in the z-direction, so that the energy difference between to states j and i will become

$$E_j - E_i = \frac{\pi^2 \hbar^2}{2m^* L^2} \left(j^2 - i^2 \right). \tag{S3}$$

Given the basis functions above and assuming full polarization of the THz field in the z-direction, we can evaluate the matrix elements via $p_z = -\mathrm{i}\hbar\, d/dz$

$$\langle \Psi_j | \mathbf{e} \cdot \mathbf{p} | \Psi_i \rangle = \langle \Psi_j | p_z | \Psi_i \rangle = -\mathrm{i}2\hbar \frac{(-1 + (-1)^{i+j})\, i\, j}{(i^2 - j^2)L} \tag{S4}$$

Equation S4 imposes a quasi selection rule within Equation 1 from the main text, as with increasing j at a fix i the matrix element drops rapidly to zero due to the denominator. Term A (Equation 1 main text) for the second dipole allowed transition $|1\rangle \rightarrow |4\rangle$ is already a factor of 30 smaller than that of the first $|1\rangle \rightarrow |2\rangle$ transition. Further higher transitions have even bigger ratios to the first transition. Hence only transitions from an initial state to the (energetically) nearest final states have considerable transition probability. We emphasize, that different confinement potentials –like a shallow well with low confinement potential– will alter e.g. the population density dependence of the mobility (see main text), as the matrix

elements above and the energy denominator in Equation 1 or 4 (main text) are altered for the concatenated states.

Equation 4 from the main text is finally retrieved, expanding the Lorentzian lineshape function. We already include the imaginary unit i from the prefactor in Equation 1 (main text) here for clearness.

$$\frac{\mathrm{i}}{E_j - E_i - \hbar\omega - \mathrm{i}\hbar\Gamma} = \underbrace{\frac{-\hbar\Gamma}{(E_j - E_i - \hbar\omega)^2 + (\hbar\Gamma)^2}}_{\text{Real Contribution to } \sigma(\omega)} + \mathrm{i}\underbrace{\frac{E_j - E_i - \hbar\omega}{(E_j - E_i - \hbar\omega)^2 + (\hbar\Gamma)^2}}_{\text{Imaginary Contribution to } \sigma(\omega)} \quad \text{(S5)}$$

S2 Phase Response

Figure S1 shows the phase angle resulting from real and imaginary electron (hole) mobilities at different nano wire length under variation of excitation frequency (a+b) and number of charge carriers (i.e. population, c+d). The phase course in (a+b) deviates from the Drude response[1] or Lorentz-oscillator model, which increases with frequency from 0 to $\pi/2$ for the former. For low T and low frequency in (a) the response is similar to a driven single harmonic oscillator, depending on the relative detuning of THz photon and transition energy. The THz radiation is strongly sub resonant to the 1D domain electronic transitions, so that a domain prolongation results in an approach to the resonance with increasing real part of the conductivity, so that the (negative) phase angle is reduced. For higher frequencies more transitions become near resonant leading to a steep slope and slight wiggles. For high THz
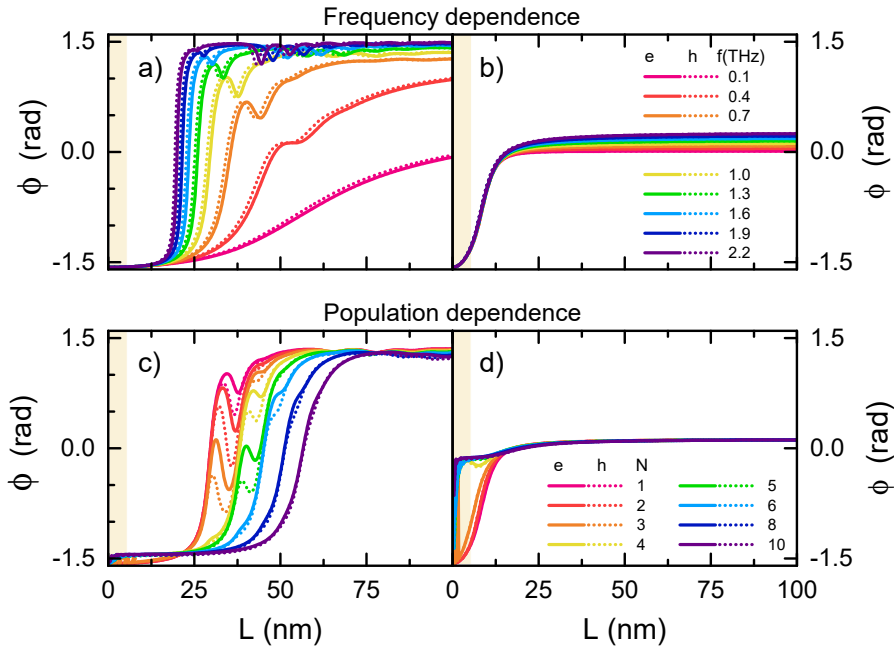

Figure S1: Length dependent Phase response for CdSe nanowires under (a) variation of excitation frequency, assuming a single electron/hole and (b) variation of population of charge carriers, assuming excitation at 1 THz.

frequencies (at 10 K), the resonance to the lowest transition is reached (near 20 nm length) and the phase is transitioning from $-\pi/2$ to $\pi/2$. This can be seen as the dephasing of $\Gamma = 8 \cdot 10^{11} \text{s}^{-1}$ at 10 K is of the same order of magnitude as the detuning $\Delta\omega = (E_j - E_i)/\hbar - \omega$, of the order of 1 THz. At elevated temperatures (300 K) this is not the case ($\Gamma = 5 \cdot 10^{13} \text{s}^{-1}$) and the dephasing dominates. Increasing dephasing and the involvement of multiple states at elevated temperature (b) results in a randomization of the total phase angle associated with a near zero value. The contribution of each additional level –approaching in energy once the wire length is increased– is added incoherently, resulting in the observed quasi zero phase for long L in (b). In case of varying number of initial charge carriers at 10 K, the excitation of 1 THz is always quasi-resonant to at least some transitions (Figure S1 c), once the a certain length (25 nm, compare to yellow curve in (a)) is reached. The higher density of states with increasing length results, as before, in wiggles and an increasing phase response. Allowing more initial charge carriers, however, elevates the Fermi level and thus only transitions of higher resonance will contribute to the real and imaginary part. This can be seen in (c), as even higher length are necessary before resonance between higher states and the 1 THz excitation is reached. In case of 300 K, as discussed before, a phase randomization occurs, which is quasi-independent of length, as the position of the very broad Fermi edge is no longer crucial for selecting specific transitions.

S3   Impact of Dephasing on $\mu(\omega)$

As an additional aspect, we investigate with respect to Equations 1 and 4 from the main text how dephasing impacts the conductivity and mobility of our nano systems. Figure S2 shows the frequency-dependent mobility of a CdSe wire of 20 nm length at various dephasing rates. A first observation is that both at low and high temperature higher dephasing increases the real mobility in our CdSe wire. For low dephasing rates the real part of the conductivity is directly proportional to the dephasing rate Γ in Equation S5 and 9 (main text). This is observed due to the fact, that the denominator is not dominated by the dephasing, but the detuning, hence in off-resonant cases. We included here the prefactor i from Equation 1 (main text) to Equation S5 to show that the dephasing Γ acts on the real part of the conductivity numerator. The negative Fermi occupation difference at finite temperature in Equation 1 and 4 (main text) results then in a positive real part of the conductivity and mobility, while the imaginary part is negative for sub resonance, see Figure S2. For the highest dephasing rate (10^{14}/s) this is e.g. not the case any more, so that the mobility does not increase with frequency till the first resonance for the real part, as the real part in Equation S5 becomes constant. Comparing further the real part for 10 K and 300 K for not excessive dephasing we see that in both cases the real part increases (in the sub resonant regime) with frequency as in Figure 1 (main text), as well as that the small effective mass difference for electron and hole results in minor changes. However, the mobilities at 300 K in Figure S2 are always lower than for 10 K, even for an identical dephasing rate, an unexpected result. Hence, it is not the result of e.g. altering phonon or impurity scattering. The reason for it relates to the Fermi occupation difference term in Equation 1 or 4 (main text). With increasing temperature the thermal Fermi distribution –which has a width of $\pm k_B T$– gets broader so that the differences in the populations for the nearest states in energy become smaller at elevated temperatures.
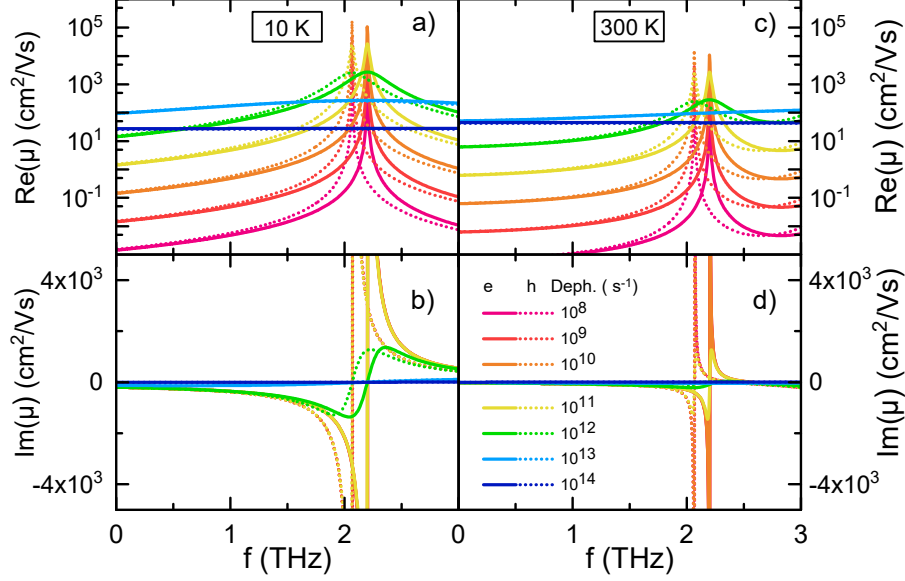
Figure S2: Frequency dependent real (a+c) and imaginary (c+d) mobility of 20 nm CdSe nanowires for varying dephasing at 10 K and 300 K under the assumption of one charge carrier per domain.

Hence the $f(E_j) - f(E_i)$ factor, that scales the matrix elements is reduced.

Further, due to the mentioned rapid decrease of the transition strength with increasing quantum number difference of initial and final state and the $E_j - E_i$ energy denominator only nearby states (j-i small) contribute significantly. These three factors together reduce the real mobility at elevated temperature by an order of magnitude, a remarkable effect, and already without the involvement of any changes in the dephasing rate by temperature dependent phonon scattering. Hence, in contrast to frequent claims in literature, the temperature dependence of the charge carrier mobility in a nanosystem is not only based on phonon or impurity scattering, but also on the thermal broadening of the Fermi edge. We remark that we use temperature-dependent dephasing rates of $8 \cdot 10^{11} s^{-1}$ at 10 K and $5 \cdot 10^{13} s^{-1}$ at 300 K in CdSe, as mentioned above, in the other figures, so that the mobility ratio between 10 and 300 K gets even bigger than by the thermal population effect only and can reach nearly two orders of magnitude (see Figure 1, main text). In the case of high dephasing the imaginary part of the mobility in Figure S2 (b+d) nearly vanishes as compared to the real part, expected from Equation S5. For decreasing dephasing its negative value increases until some saturation curve is reached, where the detuning dominates the denominator of Equation S5. Overall the negative imaginary mobility is always bigger at 10 K than at 300 K.

These effects can be also seen in the length dependencies for variable dephasing, plotted in Figure S3. Unlike Figure 2 (main text), we can observe for low dephasing each resonant transition, which adds to the total mobility, once the wire length increases and hence the THz photon energy becomes subsequently resonant to the lowest and higher transitions (Figs. S3 a,b,d,e). The real mobility is in-line with Figure S2 lower at lower dephasing and higher temperature for e.g. a fixed length of 20 nm. In the sub-resonant regime the absolute values
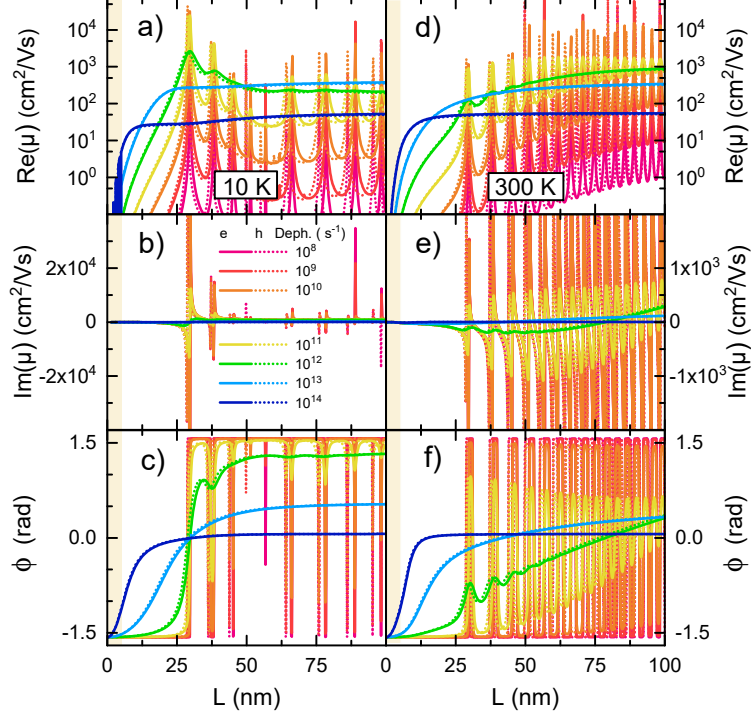
Figure S3: Lateral length dependence of the real (a+d) and imaginary (b+e) mobility as well as phase angle due to retardation (c+f) for CdSe nanowires at 10 K and 300 K under the assumption of one charge carrier per domain at 1 THz.

of real and imaginary conductivity increase with wire length. For the case of low dephasing rates sharp resonances with high mobilities occur, which result in square- or delta-like (c+f) phase responses. For dephasings of at least 10^{12}/s the course of the mobility and phase is smooth again.

S4 Comparison with Experiments

The calculation of the conductivity according to the Kubo-Greenwood model requires knowledge of the number of present charge carriers on the nanoparticle. On the one hand this is influenced by the number of absorbed pump photons in an optica pump-THz probe experiment, on the other hand will some of the initially formed electrons and holes form excitons. Hence just a fraction of excitations result in free carriers, that will exhibit their specific conductivity.

A CdSe nano rods

For calculation we use a dephasing constant of $\Gamma = 0.3 \cdot 10^{13}$ s^{-1} at room temperature,[2] and otherwise CdSe nanorod parameters as discussed in the main text. The curves in Figure 5 (main text, a+b, turqoise and orange) are obtained by scaling the modeled conductivity with the sample thickness. This is to obtain the experimentally measured sheet conductivity σ_s.[3]

We note, that the scaling factor of $\tilde{d} = 1.2$ μm contains the volume fraction ($\tilde{d} = f_V \cdot d$), as a 1 micron layer of pure CdSe nanorods would not leave any detectable terahertz radiation in the probe beam after absorption in the sample.

A.1   Number of absorbed Photons

The average number of photons absorbed by a single nanorod in a single pump excitation pulse of FWHM τ can be approximated as

$$N_{abs} = \sigma^{(1)}(\lambda) \cdot \Phi(\lambda) \cdot \tau. \tag{S6}$$

Here, $\sigma^{(1)}$ is the single photon absorption cross-section (in cm^2) and Φ the photon-flux density (in photons/m^{2}s). While Φ is linked to experimental parameters as pulse energy E_p (72 nJ)[4] and focal spot diameter d_{sp} (2.2 mm)[4] or focal spot area A_{sp} (m^2), according to

$$\phi = \frac{I}{h\,\nu} = \frac{E_p}{A_{sp}\,\tau\,h\,\nu} = \frac{4\,E_p}{\pi d_{sp}^2\,\tau\,h\,\nu}, \tag{S7}$$

the absorption cross-section is not only substance-specific, but also a particle shape-specific property, that is determined by the intrinsic absorption coefficient μ_i (3·10^7 m^{-1} from Ref. 5) and the particle volume ($V_{part} = 640$ nm^3).[4]

$$\sigma^{(1)} = \mu_i \cdot V_{part}. \tag{S8}$$

For the mentioned parameters we obtain a total number of absorbed photons per pulse of $N_{abs} = 0.73$ photons/particle.

A.2   Formation of Excitons

Initially photocreated charge carriers in a nano rod or wire will undergo exciton formation according to the 1D Saha equation.[6,7] The yield of charges and excitons at room temperature depends on the exciton binding energy–here taken as 190 meV,[8]–and is calculated as

$$\frac{n_e\,n_h}{n_x} = \frac{n_c^2}{n_x} = \left(\frac{2\mu_{eh}k_B\,T}{\pi\hbar^2}\right)^{\frac{1}{2}} \cdot e^{\frac{-E_{B,x}}{k_B\,T}}, \tag{S9}$$

$$n_c + n_x = n_{1D}, \tag{S10}$$

where $E_{B,x}$ is the exciton binding energy, μ_{eh} the reduced mass of the electron-hole-pair and n_{1D} is the 1D density of excitations $n_{1D} = N_{abs}/L$. We note, that eq. S10 does not require $n_e + n_h + n_x = n_{1D}$, as a photon creating an electron likewise generates a hole at the same time. As a result we find the fraction of charge carriers ϕ_c and excitons ϕ_x to be 4 % and 96 %. Hence, on average $N_{abs} \cdot \phi_c = 0.04$ electrons (holes) are formed per excitation on the nano rod.

A.3 Uncertainty estimation

We estimate the the impact of a length dispersion of the considered nano wires on the uncertainty $(\Delta\sigma_R)$ of the real and $(\Delta\sigma_I)$ of the imaginary conductivity in Equation 1 and 9, depending on the domain length L_z (main Text):

$$\Delta\sigma = \left(\frac{\partial\sigma}{\partial L_z}\right)\Delta L_z \tag{S11}$$

Using $V = L_x L_y L_z$, we reformulate Equation S11 for the real part as:

$$\Delta\sigma_R = -\sum_{ij}\underbrace{\frac{8q_e^2\hbar}{m^*\pi^2 L_x L_y}\frac{(-1+(-1)^{i+j})^2 i^2 j^2\hbar\Gamma}{(i^2-j^2)^3}}_{B_{ij}}\frac{\partial}{\partial L_z}\left(\frac{1}{L_z}\frac{f(E_j)-f(E_i)}{(E_0(j^2-i^2)-\hbar\omega)^2+(\hbar\Gamma)^2}\right)\Delta L_z \tag{S12}$$

Similarly, we write for the imaginary part, using the notation for the prefactor $B_{i,j}$ as above,

$$\Delta\sigma_I = \sum_{ij}B_{ij}\frac{\partial}{\partial L_z}\left(\frac{1}{L_z}\frac{(f(E_j)-f(E_i))(E_0(j^2-i^2)-\hbar\omega)^2+(\hbar\Gamma)}{(E_0(j^2-i^2)-\hbar\omega)^2+(\hbar\Gamma)^2}\right)\Delta L_z. \tag{S13}$$

B PbSe nano rods

For modeling we use $m_e^* = 0.56\ m_0$ and $m_h^* = 0.43\ m_0$,[9] as well as a typical $\Gamma = 1.4{\cdot}10^{14}$ s^{-1} for nanostructures[10–12] at room temperature. Similar to the 1D Saha Equation used for CdSe nano rods above, we calculate the fraction of charges and excitons in the PbSe nano rods, employing an exciton binding energy $E_{B,X} = 154$ meV.[7,9] Here, the number of excitations is given. Table S1 summarizes the fraction of charges (ϕ_c) and excitons (ϕ_x) for the specified datapoints (in Figure 5 (c), main text) versus the number of excitatons N_i (i.e. number of absorbed photons per particle or the sum of e-h pairs and excitons).

Table S1: Resulting fraction of charges (ϕ_c) and excitons (ϕ_x) from the 1D Saha equation for a number of absorbed photons N_i per particle .

N_i	1.5	2.2	2.8	3.1	3.5	3.9	5.6	7.9	10.1	14.2	16.3
ϕ_c	0.188	0.161	0.142	0.136	0.129	0.123	0.104	0.088	0.078	0.066	0.062
ϕ_x	0.812	0.839	0.858	0.864	0.871	0.877	0.896	0.912	0.922	0.934	0.938

After simulating the different single particle conductivity spectra $\sigma(f) = \sigma_e(f) + \sigma_h(f)$, we average over frequency to obtain $\bar{\sigma}$

$$\bar{\sigma} = \frac{\int_{0.5\,\text{THz}}^{1.2\,\text{THz}}(\sigma_e(f)+\sigma_h(f))df}{(1.2-0.5)\text{THz}}. \tag{S14}$$

Since we are interested in the mobility, we apply $\mu_{e,h} = \sigma_{e,h}V/(N_{e,h}/;q_e)$ with N_c/V as the carrier density on the nanoparticle ($V = L_x L_y L_z$). The number of carriers N_c is given by

$N_c = \phi_c \cdot N_i$. Analogue to the data from Ref. 7, we calculate the real part of the frequency averaged mobility, weighed with the fraction of carriers according to:

$$\bar{\mu} = \frac{V}{q_e\,\phi_c\,N_i}\bar{\sigma} \quad \Longrightarrow \quad \phi_c \cdot \bar{\mu} = \frac{V}{q_e\,N_i}.\bar{\sigma} \tag{S15}$$

This is then used for the comparison with data in Figure 5 c).

S5 Long Wires: Comparison with Drude- and Plasmon-Model

In the following section we will compare the results of our Kubo-Greenwood model with those from a Drude model or a Plasmon model. We will show that for long wires the classical Drude result is recovered by the the Kubo-Greenwood theory. The Drude Model (or often also Drude-Lorentz-Model) assumes a non-interacting electron-hole-gas, where the charge carrier momentum relaxation (or collision rate) is given by a parameter $\gamma = 1/\tau$. For the momentum relaxation associated scattering processes it assumes a continuum of states charge carrier states, associated with a bulk-like density of states. We will briefly derive the resultant carrier mobilities for the Drude and Plasmon model to compare them with the Kubo-Greenwood results and show that coincidence is obtained for long domain size.

The movement of an electron or hole under influence of a real external monochromatic electric field $E(t) = E_0 \cos(\omega t)$ of angular frequency ω is described by

$$\frac{d^2x}{dt^2} + \gamma\frac{dx}{dt} = \frac{q_e\,E(t)}{m^*_{e/h}}. \tag{S16}$$

As we are interested in the mobility, we use the relation $v(t) = dx(t)/dt = \mu \cdot E(t)$, defining the charge drift velocity v and mobility μ. However, we have to keep in mind, that the solutions will be obtained in the form of

$$v(t) = \frac{1}{2}E_0(\mu\,e^{-\mathrm{i}\omega t} + c.c.), \tag{S17}$$

where c.c. stands for complex conjugate. Upon solving Equation S17 one obtains after differentiating $x(t)$

$$v(t) = \frac{E_0\,q_e\,(\gamma\cos(\omega t) + \omega\sin(\omega t))}{m^*_{e/h}(\gamma^2 + \omega^2)} = \frac{q_e}{2m^*_{e/h}(\gamma^2 + \omega^2)}\left[(\gamma + \mathrm{i}\omega)e^{-\mathrm{i}\omega t} + c.c.\right], \tag{S18}$$

from which we extract the frequency-dependent mobility $\mu(\omega)$ according to Equation S17

$$\mu(\omega) = \frac{q_e\,(\gamma + \mathrm{i}\omega)}{m^*_{e/h}(\gamma^2 + \omega^2)} = \frac{q_e}{m^*_{e/h}(\gamma - \mathrm{i}\omega)} = \frac{q_e}{m^*_{e/h}}\frac{\tau}{1 - \mathrm{i}\omega\tau}, \tag{S19}$$

where we obtain the in literature well-known $\sigma(\omega)$, when applying $\sigma = q_e\,n_{e/h}\,\mu$.[1]

In a similar manner, we can generate a solution for the Plasmon model, which is extending

the equation of motion (Equation S16) by a restoring force term $\omega_0^2 x$:

$$\frac{d^2 x}{dt^2} + \gamma \frac{dx}{dt} + \omega_0^2 x = \frac{q_e \, E(t)}{m_{e/h}^*} \tag{S20}$$

Proceeding with the solution of this driven damped oscillator like before, the mobility is obtained as

$$\mu(\omega) = \frac{q_e}{m_{e/h}^*} \frac{\tau}{1 - \mathrm{i}\tau(\omega - \omega_0^2/\omega)} = \frac{q_e}{m_{e/h}^*} \frac{1}{\gamma - \mathrm{i}(\omega - \omega_0^2/\omega)}. \tag{S21}$$

While in the Drude-Model a charge undergoes a driven oscillation with and dissipates its kinetic energy to a reservoir within an average scattering time τ, the charged particle experiences an additional restoring force $m^* \omega_0^2 x$ in the Plasmon-model. The Drude-Model can thus be understood as the limiting case of the Plasmon-model, with zero restoring force, implying $\omega_0 = 0\,\mathrm{THz}$.

In the following we discuss the results of the different models - Kubo-Greenwood, Drude and Plasmon - obtained by assuming a 10 nm and 80 nm nano rod at 300 K. The procedure is such, that we generate with the Kubo-Greenwood model ($\Gamma = 5 \cdot 10^{13}/\mathrm{s}$, 40 states, 1 electron/hole per nano rod) data and subsequently fit them by Equations S19 and S21 in a global manner for real and imaginary part. Figure S2 shows the resulting curves for the 10 and 80 nm simulated data, always divided in the real part of μ (a+d), the imaginary part (b+e) and the phase, defined as $\arctan(\mathrm{Im}(\mu)/\mathrm{Re}(\mu))$ (c+f).

The obtained fitting parameters (always identical for Re and Im) are shown in Table S2. As seen from the results and Figure S2 (a+b+c) the agreement of either of the three models is low for 10 nm nano rod length. This is understood, as for a small nano particles the energetic spacing between adjacent discrete states is high. Since both, the Drude- and Plasmon-Model assume a continuum of states inherently, the mismatch is large. However, it is noteworthy, that the resonance frequency f_0 predicted by the Plasmon-model at 10 THz resides in-between the two lowest neighboring transition frequencies f_{21} and f_{32} of 8.8 and 14.7 THz in the nano rod, which have presumably the strongest contribution in rods with such strong lateral confinement. Summing up, for short nanostructures the quantized nature of the energy levels makes a treatment of the frequency dependent mobility by the Kubo-Greenwood approach necessary.

Table S2: Fitting parameters for Drude- and Plasmon-model for nano rods of 10 and 80 nm length.

Length		τ (fs)	Γ or γ ($10^{13}/\mathrm{s}$)	$f_0 = 2\pi\omega_0$ (THz)
	Kubo	20	5	-
10 nm	Drude	4.6	21.7	-
	Plasmon	8.5	11.8	10
	Kubo	20	5	-
80 nm	Drude	18.5	5.4	-
	Plasmon	18.2	5.5	0.07

Proceeding to the case of a longer nano wire, the agreement of each model with the Kubo-Greenwood simulations is very high. Especially once the obtained scattering rates γ are compared to Γ, assumed in the Kubo-Greenwood model. This is understandable, as for longer wires the energy spacings of the discrete states are strongly reduced and indeed a quasi continuum of states is involved. It results from the state broadening by dephasing as well as the thermal distribution of population at room temperature. The mean scattering constants γ from Drude- and Plasmon-model are in good agreement with the dephasing constant Γ put into the model (Table S2). For even longer wires the results approach each other asymptotically, due to the more end more continuous density of states.

While the phase response showed no agreement for small rods (10 nm) in c), in the case of 80 nm the phase curves overlap in the entire frequency spectrum (f). Also the $\pi/2$ phase, resulting in a zero amplitude at high frequencies, is reproduced in f).
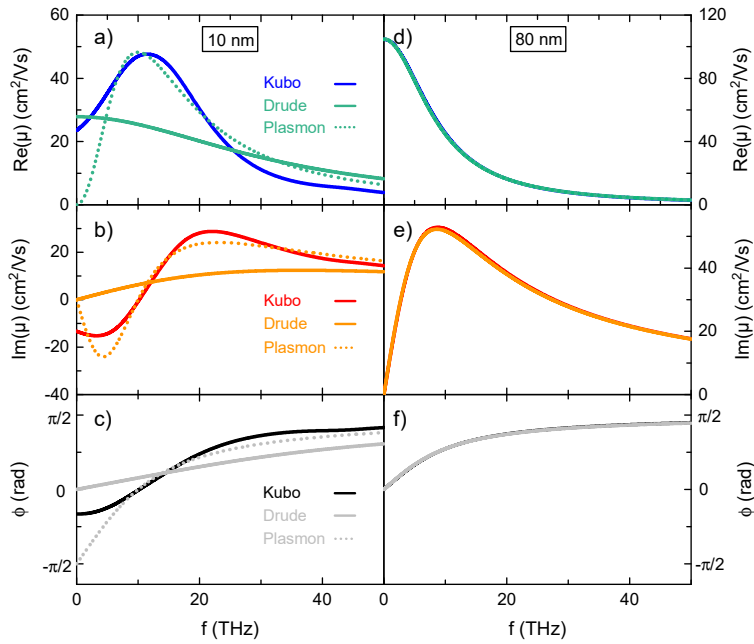

Figure S4: Comparison of Kubo-Greenwood- with Drude- and Plasmon-model for 10 nm and 80 nm long nano rods.

This comparison clearly shows, that the classical limit of the Kubo-Greenwood Theory at wire lengths coincides with Drude- and Plasmon-model predictions and that the parameters obtained from fitting do have a meaning in the sense of the Kubo-Greenwood theory. Nonetheless, it has to be emphasized strongly, that this is not the case for small particles. The large energy spacing forbids, even with the broad thermal broadening at room temperature, a treatment as a continuum of states and the charge carrier motion can only be modeled in a quantum mechanical approach, as proposed by our Kubo-Greenwood model. Finally, we remark that this statement is especially also valid at low temperatures, when thermal broadening of the states and broadening by thermal population is low. There the the system can remain in a quantum regime of transport –distinct from Drude or Plasmon models– even for longer nano wires.

S6 Guidlines for analysis of experimental THz-mobility spectra

If it is desired to analyze and fit experimentally obtained conductivity or mobility spectra, e.g. from optical-pump THz-probe spectroscopy, the following steps may be applied to compare these spectra to our model.

- Determine system size (e.g. by TEM) and from that the normalization volume V for Equation (1) and (4)

- Determine the ground state and eigen energies of the electronic system E_i as given in the main text or Equation S2 (ESI).

- Determine the density of excitations per nanorod. The number of absorbed photons (see section A.1 of ESI) needs to be determined based on the experimental conditions. Subsequently the fraction of excitons and electron-hole-pairs is determined via the Saha-Equation (see section A.2. of ESI). This results in N, the number of negative (and positive) charge carriers on the domain.

- Determine the population dependent Fermi Energy E_F according to Equations (2) and (3).

- Determine the occupation number $f(E_i)$ for each state to be considered. As a measure of accuracy of the simulation, sum up the Fermi occupations $\sum_{i=1}^{i_{max}} f(E_i) = N \cdot \xi$. Here, ξ is a measure of the accuracy of the mapping of the population on i_{max} electronic states considered in the simulation. This determines the size of the initial basis. Reasonable choices could be 0.99 or 0.95 depending on the computational performance.

- Calculate all transition dipole moments for the mentioned basis according to Equation S4 (ESI).

- Using Equation (4) (main text) the dipole moments and eigen energies are already included in the summation.

- As reflected in Equations (1) and (4) a summation over all initial and final state combinations has to be evaluated from the lowest state with $i = 1$ or $j = 1$ to $i_{max} = j_{max}$. With the resultant equation a fit to experimental data may be performed.

References

(1) Lloyd-Hughes, J.; Jeon, T.-I. A Review of the Terahertz Conductivity of Bulk and Nano-Materials. *Journal of Infrared, Millimeter, and Terahertz Waves* **2012**, *33*, 871–925.

(2) Wen, X.; Sitt, A.; Yu, P.; Toh, Y.-R.; Tang, J. Temperature dependent spectral properties of type-I and quasi type-II CdSe/CdS dot-in-rod nanocrystals. *14*, 3505–3512.

(3) Datta, S. *Lessons from Nanoelectronics*, 2nd ed.; World Scientific.

(4) Cooke, D.; Lek, J. Y.; Krebs, F.; Lam, Y.-M.; Jepsen, P. Time-resolved terahertz spectroscopy of conjugated polymer/CdSe nanorod composites. **2010**, *7600*.

(5) Achtstein, A. W.; Antanovich, A.; Prudnikau, A.; Scott, R.; Woggon, U.; Artemyev, M. Linear Absorption in CdSe Nanoplates: Thickness and Lateral Size Dependency of the Intrinsic Absorption. *The Journal of Physical Chemistry C* **2015**, *119*, 20156–20161.

(6) Ambigapathy, R.; Bar-Joseph, I.; Oberli, D. Y.; Haacke, S.; Brasil, M. J.; Reinhardt, F.; Kapon, E.; Deveaud, B. Coulomb Correlation and Band Gap Renormalization at High Carrier Densities in Quantum Wires. *Phys. Rev. Lett.* **1997**, *78*, 3579–3582.

(7) Kulkarni, A.; Evers, W. H.; van Waas, T. P.; Siebbeles, L. D. A. Photogeneration Quantum Yield and Character of Free Charges and Excitons in PbSe Nanorods. *The Journal of Physical Chemistry C* **2020**, *124*, 7550–7557.

(8) Rajadell, F.; Climente, J.; Planelles, J.; Bertoni, A. Excitons, Biexcitons, and Trions in CdSe Nanorods. *The Journal of Physical Chemistry C* **2009**, *113*, 11268.

(9) Bartnik, A. C.; Efros, A. L.; Koh, W.-K.; Murray, C. B.; Wise, F. W. Electronic states and optical properties of PbSe nanorods and nanowires. *Phys. Rev. B* **2010**, *82*, 195313.

(10) Kamisaka, H.; Kilina, S. V.; Yamashita, K.; Prezhdo, O. V. Ultrafast Vibrationally-Induced Dephasing of Electronic Excitations in PbSe Quantum Dots. *6*, 2295–2300.

(11) Prezhdo, O. Multiple Excitons and the Electron-Phonon Bottleneck in Semiconductor Quantum Dots: An Ab Initio Perspective. *460*.

(12) Neukirch, A. J.; Neumark, D. M.; Kling, M. F.; Prezhdo, O. V. Resolving multi-exciton generation by attosecond spectroscopy. *22*, 26285–26293.